



1

2 **Deep-Learning-derived Planetary Boundary Layer Height from**

3 **Conventional Meteorological Measurements**

4

5 Tianning Su^{1*}, Yunyan Zhang¹

6

7 ¹Lawrence Livermore National Laboratory, Livermore, CA, USA

8

9

10

11

12

13

14

15 **Correspondence to: su10@llnl.gov*

16

17

18

19

20



21 **Abstract.** The planetary boundary layer (PBL) height (PBLH) is an important
22 parameter for various meteorological and climate studies. This study presents a multi-
23 structure deep neural network (DNN) model, designed to estimate PBLH by integrating
24 morning temperature profiles with surface meteorological observations. The DNN
25 model is developed by leveraging a rich dataset of PBLH derived from long-standing
26 radiosonde records and augmented with high-resolution micro-pulse lidar and Doppler
27 lidar observations. We assess the performance of the DNN with an ensemble of ten
28 members, each featuring distinct hidden layer structures, which collectively yield a
29 robust 27-year PBLH dataset over the Southern Great Plains from 1994 to 2020. The
30 influence of various meteorological factors on PBLH is rigorously analyzed through
31 the importance test. Moreover, the DNN model's accuracy is evaluated against
32 radiosonde observations and juxtaposed with conventional remote sensing
33 methodologies, including Doppler lidar, ceilometer, Raman lidar, and Micro-pulse
34 lidar. The DNN model exhibits reliable performance across diverse conditions and
35 demonstrates lower biases relative to remote sensing methods. In addition, the DNN
36 model, originally trained over a plain region, demonstrates remarkable adaptability
37 when applied to the heterogeneous terrains and climates encountered during the
38 GoAmazon (Tropical Rainforest) and CACTI (Middle Latitude Mountain) campaigns.
39 These findings demonstrate the effectiveness of deep learning models in estimating
40 PBLH, enhancing our understanding of boundary layer dynamics with implications for
41 enhancing the representation of PBL in weather forecasting and climate modeling.

42



43 1 Introduction

44 The Planetary Boundary Layer (PBL) is the atmosphere's lowest part, where the
45 Earth's surface directly influences meteorological variables, impacting the climate
46 system (Garratt, 1994; Kaimal and Finnigan, 1994). The PBL height (PBLH) is a
47 meteorological factor that strongly influences surface-atmosphere exchanges of heat,
48 moisture, and energy (Stull, 1988; Caughey, 1984; Holtslag and Nieuwstadt, 1986;
49 Mahrt, 1999; Helbig et al., 2021; Guo et al., 2024; Beamesderfer et al., 2022). In
50 addition, PBLH it is a crucial variable for monitoring and simulating surface pollutant
51 behaviors since it determines the volume available for near-surface pollutant dispersion
52 (Li et al., 2017; Su et al., 2022a; Tucker et al., 2009). Due to its impacts on the
53 development of convective systems, PBLH is also a key parameter in numerical
54 weather forecasts and climate models (Menut et al., 1999; Park et al., 2001; 2023;
55 Emanuel, 1994; Guo et al., 2017; Lilly, 1968; Matsui et al., 2004).

56 Radiosonde (SONDE) remains the standard method for estimating PBLH, yet it is
57 hampered by limitations in temporal frequency, restricting its ability to
58 comprehensively capture the whole diurnal cycle of PBL development (Stull, 1988;
59 Seidel et al. 2010; Guo et al. 2021; Liu and Liang, 2010). To overcome these challenges,
60 there has been an increasing dependence on remote sensing techniques, especially lidar
61 systems. These techniques capture atmospheric vertical information (e.g., aerosols,
62 temperature, humidity, and wind) at high temporal and vertical resolutions, leading to
63 remote sensing-based retrievals of PBLH (Menut et al., 1999; Kotthaus et al., 2023;
64 Sawyer and Li, 2013). The remote sensing systems, including Doppler lidar (Barlow et



65 al. 2011), ceilometer (Zhang et al. 2022), Raman lidar (Summa et al. 2013), and Micro-
66 pulse lidar (Melfi et al., 1985), utilize laser-based technology to track PBLH diurnal
67 evolutions, helping us understand the PBL dynamics (Cohn and Angevine, 2000; Davis
68 et al., 2000).

69 Despite advancements in remote sensing for PBLH estimation, challenges persist
70 in aligning the results from various remote sensing instruments with those from
71 SONDE measurements (Zhang et al. 2022; Su et al. 2020; Chu et al., 2019).
72 Specifically, interpreting aerosol, turbulence, and moisture profiles derived from
73 remote sensing techniques to determine PBLH bears inherent limitations due to the
74 unstable signal-to-noise ratio (Su et al., 2017; Kotthaus et al., 2023; Krishnamurthy et
75 al., 2021). This issue is compounded by the differing measurement methodologies
76 employed by various remote sensing tools, leading to notable uncertainties when
77 comparing their PBLH estimates to those obtained from standard SONDE retrievals
78 (Zhang et al. 2022; Sawyer and Li, 2013).

79 As machine learning (ML) has shown potential in atmospheric science (McGovern
80 et al., 2017; Gagne et al., 2019; Vassallo et al., 2020; Cadeddu et al., 2009; Molero et
81 al. 2022), this technique presents a promising tool for refining the estimation of PBLH
82 to resolve the inherent complexity and variability of PBL. For example, several studies
83 use ML to identify PBL heights using thermodynamic profiles or backscatter profiles
84 from Lidar or Atmospheric Emitted Radiance Interferometer (AERI), highlighting the
85 ML's superiority over conventional techniques under different scenarios (Sleeman et al.
86 2020; Krishnamurthy et al., 2021; Rieutord et al. 2021; Liu et al. 2022; Ye et al. 2021).



87 Moreover, Li et al. (2023) used an ML algorithm that considers the vertical distribution
88 of aerosols to find the PBLH under complex atmospheric conditions.

89 While existing ML methodologies have marked progress in estimating PBLH, these
90 studies mainly focus on refining retrievals from remote sensing data, particularly lidar-
91 based technologies. Thus, there is an inherent limitation to the applicability due to a
92 reliance on specific remote sensing instruments. To address this issue, we aim to
93 leverage and integrate the comprehensive field observations (i.e., radiosonde and
94 remote sensing techniques) to develop a deep learning model for direct PBLH
95 estimation from conventional meteorological data. This strategy circumvents the
96 limitations of relying on particular remote sensing technologies. Furthermore, our
97 model employs a multi-structure deep neural network (DNN), diverging from
98 traditional ML methods like random forest, to enhance its adaptivity for PBLH
99 estimations. This multi-structure DNN approach offers great potential for wide
100 applications under various meteorological conditions, as well as a stable performance
101 for both trained and untrained periods. This underscores the versatility of DNN as a tool
102 for PBLH estimation, which can be utilized under different scenarios and locations.

103 By focusing on the interaction between surface meteorology and the PBL, this study
104 introduces a DNN-based method to estimate the daytime evolution of PBLH from
105 morning temperature profiles and surface meteorology. We evaluate the model's
106 performance using extensive datasets over the Southern Great Plains (SGP) for a period
107 spanning 27 years (1994-2020) and includes comparisons with PBLH estimations
108 obtained from Doppler lidar, ceilometer, Raman lidar, and micro-pulse lidar.



109 Furthermore, we explore the generalizability of the model to different geographic
110 regions and climates, as tested during the field campaigns, e.g., Green Ocean Amazon
111 (GoAmazon) and Cloud, Aerosol, and Complex Terrain Interactions (CACTI).

112

113 **2 Data and instruments**

114 **2.1 ARM Sites**

115 The Atmospheric Radiation Measurement (ARM) program, funded by the U.S.
116 Department of Energy, has been employed at the Southern Great Plains (SGP) site in
117 Oklahoma (36.607°N, 97.488°W) for several decades. This study use comprehensive
118 field observations at the SGP site during 1994 to 2020. In addition to the SGP site, this
119 study utilizes data from the ARM GoAmazon (3.213°S, 60.598°W) and ARM CACTI
120 (32.126°S, 64.728°W) field campaigns to carry out independent tests for the deep
121 learning model. Specifically, the GoAmazon campaign is located in the amazon tropical
122 forests and provides rich field observations data during 2014-2015. Meanwhile, the
123 CACTI central site, at an elevation of 1141 meters within the Sierras de Córdoba
124 Mountain range in north-central Argentina, offers the observations during the 2018-
125 2019 period. Utilizing these comprehensive ARM datasets, our study includes
126 thermodynamic profiles derived from radiosondes, data from the Active Remote
127 Sensing of Clouds (Clothiaux et al. 2000, 2001; Kollias et al. 2020), in-situ surface
128 flux measurements, and standard meteorological observations at the surface, as
129 documented by Cook (2018) and Xie et al. (2010).



130 SONDE measurements at the ARM sites launch routinely several times a day and
131 provide detailed information into the thermodynamic conditions of the atmosphere. The
132 technical details of the ARM SONDE data are documented in Holdridge et al. (2011).
133 Moreover, we use the surface meteorological parameters at the standard meteorological
134 station. In-situ measurements at 2 meters above ground level provide data on
135 temperature, relative humidity, and vapor pressure. Moreover, this study obtain the
136 surface sensible and latent heat fluxes the surface instruments (Wesely et al., 1995). In
137 SGP, we use the best-estimate surface fluxes in the Bulk Aerodynamic Energy Balance
138 Bowen Ratio (BAEBBR) product, which is derived from the measurements by Energy
139 Balance Bowen Ratio (EBBR). Due to the availability, we utilize the surface fluxes
140 from Quality Controlled Eddy CORrelation (QCECOR) datasets from CACTI and
141 GoAmazon sites (Tang et al. 2019).

142

143 **2.2 Existing PBLH datasets over the ARM sites**

144 For analyzing PBLH, we have utilized a variety of datasets to get a full picture of
145 PBLH derived from different instruments. These datasets are developed by using
146 different methodologies and instruments and jointly offer a detailed information of
147 PBLH under various meteorological conditions. Among these datasets, SONDE- and
148 ceilometer-derived PBLH are available for all three sites, other datasets are only
149 available over the SGP. The technique details for these datasets can be found in the
150 corresponding publications or technique reports.

151 *(1) SONDE-derived PBLH by Liu and Liang (2010):*



152 PBLHs are retrieved using a method developed by Liu and Liang (2010), based on
153 potential temperature gradients from SONDE. We focus on daytime data during 05:00–
154 18:00 Local Time (LT), with a resampled vertical resolution of 5-hPa. The SONDE
155 dataset is available at DOI: <https://doi.org/10.5439/1595321>.

156 *(2) Doppler Lidar-derived PBLH by Sivaraman and Zhang (2021):*

157 Doppler lidar PBLH estimates are derived using a vertical velocity variance method
158 during 2010-2019 (Tucker et al., 2009; Lareau et al., 2018; Sivaraman and Zhang 2021).
159 The dataset is available at DOI: <https://doi.org/10.5439/1726254>.

160 *(3) Combined MPL and SONDE PBLH by Su et al. (2020):*

161 We utilize a PBLH dataset that merges lidar and SONDE measurements during
162 1998-2023, ensuring vertical coherence and temporal continuity (Su et al. 2020). An
163 additional method for handling cloudy conditions is detailed in Su et al. (2022b). The
164 dataset is available at DOI: <https://doi.org/10.5439/2007149>.

165 *(4) Ceilometer-derived PBLH by Zhang et al. (2022):*

166 The Vaisala CL31 ceilometer, with a 7.7 km vertical range, provides detailed
167 backscatter profiles used for PBLH estimation via gradient methods during 2011-2023
168 (Zhang et al. 2022). Enhanced algorithms ensure robust estimations under all weather
169 conditions. The dataset is available at DOI: <https://doi.org/10.5439/1095593>.

170 *(5) MPL-derived PBLH by Sawyer and Li (2013):*

171 Micropulse lidar (MPL) is utilized for its high temporal resolution to retrieve PBLH
172 during 2009-2020. MPL-derived PBLH, validated against SONDE and infrared
173 spectrometer (AERI) data, improves understanding of boundary-layer processes



174 (Sawyer and Li, 2013). The dataset is available at DOI:
175 <https://doi.org/10.5439/1637942>.

176 (6) *Combined Raman Lidar and AERI PBLH by Ferrare (2012)*:

177 PBLH is calculated using merged potential temperature profiles from Raman lidar
178 and AERI, with criteria established for the SGP site. PBL heights are computed hourly
179 for 2009-2011. The dataset is available at DOI: <https://doi.org/10.5439/1169501>.

180 In the datasets, (1-3) serve as the foundation for training. Concurrently, considering
181 radiosonde as the benchmark standard, we utilized dataset (1) for validating PBLH
182 retrievals obtained from various sources. Meanwhile, datasets (4-6) are used for the
183 intercomparisons between PBLH derived from DNN and remote sensing techniques.

184

185 **3 Deep Learning Model to Estimate PBLH**

186 **3.1 The Multi-Structure Deep Learning Model**

187 Our deep learning model for estimating PBLH leverages the robustness of ensemble
188 learning using a multi-structure DNN (Sze et al. 2017; Schmidhuber, 2015; Nielsen,
189 2015; Pang et al. 2020). This model used the TensorFlow Package, developed by
190 Google (Abadi et al., 2016; <https://www.tensorflow.org/>). By employing an array of
191 varied network architectures, we capitalize on the unique strengths of each structure to
192 synthesize a more accurate and reliable estimation of PBLH. Figure 1 outlines the
193 DNN's comprehensive design, beginning with the input layer that ingests a suite of
194 morning meteorological features. We first present a preliminary run for the model to
195 obtain the importance of each input feature. Then, these inputs undergo a filtration



196 process based on their importance (Date and Kikuchi, 2018; Altmann et al. 2010),
197 ensuring that only the impactful data guide the model (detailed in Section 3.3).
198 Subsequently, the filtered inputs traverse through an ensemble of ten structures with
199 distinct hidden layers. Each structure here represents an ensemble member and
200 contributes to the prediction of PBLH in its unique way (Ganaie et al. 2022). The
201 ensemble employs a three-layer base structure [52, 28, 16] for neural networks, from
202 which ten unique configurations are derived by applying random perturbations to the
203 default settings of the base structure. These different structures for ensembles 1-10 are
204 presented in Table 1.

205 At the final stage, the model use the PBLH esimations from different ensembles to
206 get a mean value as the final PBLH retrieval. This process allows the model to leverage
207 the different results of all structures and enhance the generalizability of results. In the
208 DNN model, neuron biases in the output and hidden layers are important for the
209 network's architecture (Battaglia et al. 2018). These biases serve as fine-tuning
210 parameters to adjust the activation thresholds of neurons in different layers and further
211 refine the model's predictive capabilities. Neuron biases are initialized with small
212 random values at the start of the training process and then iteratively adjusted according
213 to the network weights during the training. Normalization is a preprocessing technique
214 that often leads to improvements in model training by scaling the input features and
215 target values to a standard range (Raju et al. 2020). The normalization process was
216 applied to each input data to ensure that they have a zero mean and a standard deviation



217 of one, as well as the target data. This standardization scales the different input data to
218 a similar range, and thus, contributes a more stable and efficient training process.

219 The hidden layers of the DNN model incorporate L2 regularization to curtail
220 overfitting, while batch normalization aids in stabilizing learning. Moreover, a dropout
221 rate of 0.2 helps the model to generalize better by reducing reliance on any specific
222 neurons during training. We choose the Adam optimizer and mean squared error as the
223 loss function, which aligns with one of the best practices for regression models (Zhang.
224 2018). The mean absolute error is selected as a metric to evaluate the model's accuracy
225 during the training. We incorporate the early stopping and learning rate reduction
226 callbacks in in the model's training for regularization and fine-tuning (Liu et al. 2019).
227 Such measures ensure optimal performance by terminating training at the right juncture
228 and avoid the overfitting in the final results.

229

230 **3.2 Training the DNN Model**

231 The training of the DNN model was conducted using a PBLH dataset enriched by
232 SONDE and lidar measurements during 1994 to 2016 over the SGP. Table 2 presents
233 the distribution of dataset samples under different local time, which were important for
234 both the training and validation processes of the DNN model. The primary dataset (i.e.,
235 PBLH derived from SONDE measurements) is listed in the first column and are
236 available routinely for 5, 11, and 17 LT. The training dataset was augmented with the
237 combined MPL-SONDE PBLH dataset (Su et al. 2020) and the Doppler Lidar-derived
238 PBLH (Sivaraman and Zhang, 2021) to address the gaps where SONDE measurements



239 were not available. In instances where radiosonde data are unavailable, the lidar datasets
240 are used for training, contingent upon their agreement with radiosonde measurements
241 within a margin of 0.2 km over a 3-hour window.

242 For the purpose of training the DNN model, 70% of the hourly data from both
243 SONDE and the lidar combined dataset were randomly selected. The remaining 30%
244 dataset, comprises the portion of SONDE measurements set aside for validation
245 purposes, including a separate subset from the years 2017 to 2020 to test the model's
246 predictive capabilities on independent data. This training and validation scheme ensures
247 that the DNN model is not only well-trained but also thoroughly evaluated, reinforcing
248 its reliability in accurately estimating PBLH. As morning SONDE data constitute the
249 primary input and boundary conditions for the model, the validation of PBLH retrievals
250 is consequently confined to the 08:00 to 18:00 LT.

251

252 **3.3 Feature Importance Score**

253 In the DNN model, we quantified the significance of each input parameter using the
254 permutation importance technique, which is a widely-used method for the deep learning
255 (Date and Kikuchi, 2018; Altmann et al. 2010). Initially, we carry out a test run to
256 determine a baseline performance by calculating the mean absolute error (MAE) on the
257 validation set. Then, each feature within this set was then individually shuffled, severing
258 its correlation with the target PBLH, and the MAE was recalculated. Compared to the
259 baseline performance, the increase in MAE from this shuffled state indicates the
260 feature's predictive value: the greater the increase, the more significant the feature. We



261 repeat this shuffling and evaluation for 15 times, each with a unique random seed to
262 ensure statistical robustness. Furthermore, we calculated the average MAE increase
263 across these iterations as the importance score. Therefore, we derived a composite
264 importance metric for feature groups to represent their significance.

265 Figure 2 presents the importance scores to demonstrate each primary feature's
266 relative influence on the model's performance. Prominently, features such as the
267 boundary layer height derived from parcel methods (BLH_{parcel}), morning potential
268 temperature profiles (θ), and surface relative humidity are identified as pivotal, with
269 their substantial impact on the accuracy of PBLH estimation being highlighted.
270 BLH_{parcel} is defined as the height where the morning potential temperature first
271 exceeds the current surface potential temperature by more than 1.5 K (Holzworth, 1964;
272 Chu et al., 2019). Complementing this, Table 3 offers an exhaustive breakdown of
273 importance scores for all considered input features within the deep learning model. In
274 refining the model, features contributing a negligible or negative effect on performance
275 (i.e., importance scores less than zero) are excluded. As a result, this selection criterion
276 has led to the inclusion of 58 out of the original 64 features. This process ensures we
277 only use inputs with a proven positive influence in the DNN model.

278

279 **4 Evaluation of Deep Learning Model**

280 **4.1 Comparative analysis of biases among different datasets**

281 A critical component of evaluating our deep learning model's efficacy is analyzing
282 the biases of individual ensemble members and their collective output. Figure 3 offers



283 a visual assessment of the mean absolute error (MAE), root mean square error (RMSE),
284 and correlation coefficient (R) for each ensemble member, alongside a comparison with
285 the ensemble mean (average of all individual ensemble members). The plotted data
286 points reveal the variation in performance across different model architectures, while
287 the ensemble mean, represented by the horizontal dashed lines, indicates the collective
288 accuracy of the ensemble approach. The structures of different hidden layer
289 configurations are listed in the Table 1.

290 This methodological consolidation results in a more reliable and accurate PBLH
291 estimation, leveraging the strengths and mitigating the weaknesses of individual
292 models. By integrating multiple neural network configurations, we revealed that an
293 ensemble prediction that consistently outperforms the individual models. This strategy
294 can improve the MAE by up to 4.4%, rendering the model less dependent on any
295 specific structural configuration.

296 An in-depth comparative analysis of biases among various PBLH estimation
297 methods is essential for validating the reliability and accuracy of the DNN developed
298 in this study. Figure 4 illustrates the MAE trends for several methods over a multi-year
299 span, with the SONDE-derived PBLH serving as the benchmark for ground truth. The
300 analysis reveals the performance of different methodologies: the DNN approach,
301 doppler lidar, ceilometer, MPL, and Raman lidar. Significantly, the DNN model,
302 depicted in black, maintains a consistent MAE trend throughout the trained period
303 (1994-2016) as well as the subsequent untrained period (2017-2020), demonstrating
304 robust predictive stability. In contrast, the remote sensing-based methods show a



305 reduction in bias from 2010 to 2022, possibly due to the improvement of remote sensing
306 data quality. The discrepancy in PBLH estimates between the DNN and SONDE
307 remains consistently lower than those observed with conventional remote sensing
308 techniques.

309 Figure 5 provides a detailed evaluation of the DNN model in comparison to
310 ceilometer and doppler lidar-derived PBLH, as these two methods have demonstrated
311 the high quality with more than nine years of datasets. Figure 5a-b contrast the PBLH
312 predictions from the DNN model for both the trained period (1994-2016) and untrained
313 periods (2017-2020), respectively, showcasing strong correlations and low MAEs,
314 indicative of the model's robust training and generalization capabilities. Figure 5c-d
315 further this examination with ceilometer and Doppler lidar comparisons, respectively.
316 Overall, Doppler lidar exhibits a closer alignment with SONDE-derived PBLH than the
317 ceilometer. However, the MAE from Doppler lidar-based estimates is still
318 approximately 48% higher than those derived from the DNN model. The correlation
319 coefficient for the DNN-derived PBLH estimates has seen a substantial improvement,
320 rising from the 0.5-0.6 range typically observed with remote sensing-based PBLH
321 methods to exceed 0.8 when compared to SONDE-derived PBLH measurements. This
322 comparative analysis not only confirms the DNN model's accuracy but also offers
323 insights into the relative performance of various contemporary PBLH estimation
324 methodologies.

325



326 **4.2 Performances of PBLH retrievals under different conditions**

327 The performance of PBLH retrievals under varying atmospheric conditions is a
328 crucial aspect of model evaluation. In Figure 6, the seasonal diurnal cycles of PBLH
329 estimated by different methods are presented, offering information into the diurnal and
330 seasonal evolution of PBL. As PBLH demonstrates notable variations for different
331 seasons and local time with large differences between summer and winter, the DNN
332 and Doppler lidar estimates show good agreement and closely track the variations
333 observed in SONDE data. Meanwhile, the ceilometer presents an underestimation of
334 PBLH, especially for the summer afternoon, indicating the potential bias of ceilometer
335 derived PBLH under a convective environment.

336 Figure 7 illustrates the diurnal variation in the model's performance by comparing
337 the correlation coefficient, RMSE, and MAE against SONDE-derived PBLH as the
338 reference. The bar graphs for each local time hour offer a comparison of the RMSE and
339 MAE, as well as the correlation, showcasing the model's precision and consistency
340 relative to remote sensing methods (i.e., ceilometer and Doppler lidar). The ceilometer-
341 derived PBLH exhibits the greatest variations during different hours, particularly
342 around noon, suggesting a time-dependent bias in its measurements. Conversely, both
343 the DNN and Doppler lidar-derived PBLH demonstrate stable performance in term of
344 MAE and RMSE throughout the day. Regarding the correlation, remote sensing
345 methods like ceilometer and Doppler lidar exhibit a lower correlation with SONDE-
346 derived PBLH, especially in the early hours (8-9 LT) with a value of 0.1-0.3, indicating
347 potential limitations in their reliability during these times. On the other hand, the DNN



348 model shows a relatively good correlation with SONDE retrievals (above 0.6 under
349 different hours). This comparison shows the efficacy of DNN in tracking the diurnal
350 cycle of PBLH.

351 Continuing our assessment of the DNN model, we analyze the DNN model's
352 monthly performance in estimating PBLH, as shown in Figure 8. The analysis compares
353 MAE, RMSE, and correlation coefficients for each month to assess the model's
354 precision and dependability. The summer months (June-July-August) exhibit higher
355 biases, with MAE values for the DNN, ceilometer, and Doppler lidar at 0.3 km, 0.56
356 km, and 0.45 km, respectively. In contrast, the winter months (December-January-
357 February) show reduced biases, with MAE values of 0.2 km for the DNN, 0.27 km for
358 the ceilometer, and 0.24 km for the Doppler lidar. Specifically, the DNN model shows
359 a much lower bias during the summer season. Compared to the remote sensing-based
360 retrievals, the DNN-derived PBLH shows a much better agreement with SONDE-
361 derived PBLH, increasing from 0.3-0.6 to approximately 0.8 in term of correlation
362 coefficients.

363 Figure 9 presents the biases of PBLH retrievals under clear-sky and low cloud
364 conditions. We calculated biases as the absolute deviation from the mean PBLH for
365 each condition, focusing particularly on the differences between low cloud (maximum
366 cloud fraction between 0-4 km exceeding 1%) and clear-sky (total cloud fraction below
367 1%) scenarios. The violin plots in this figure illustrate the data distribution of biases for
368 each method to demonstrate their variability. For the DNN model and ceilometer, the
369 relative biases between clear and cloudy conditions are comparable and the difference



370 is less than than 1%. This suggests a consistent performance across these atmospheric
371 states. However, the Doppler lidar exhibits a larger disparity, showing a 5.5% bias
372 under cloudy conditions compared to clear skies. Moreover, the spread of biases
373 (shaded areas and error bars) is notably wider for both the ceilometer and Doppler lidar.
374 This indicates large variability in their performance. For all three methods, the mean
375 biases are notably higher than the median values. Such differences indicate that the
376 mean values are notably influenced by outliers under both clear-sky and cloudy
377 conditions.

378 The analyses presented in this section illustrate the effectiveness of the DNN model
379 in capturing the PBLH variations across different local times, seasons, and atmospheric
380 conditions. Compared to the traditional remote sensing methods, the DNN model
381 exhibits relatively good accuracy in aligning with SONDE-derived PBLH, indicating
382 its capability and stable performance under different scenarios.

383

384 **4.3 Testing the DNN Model's Adaptability**

385 The DNN model relies on the incorporation of morning temperature profiles as
386 inputs, such as detailed in Table 3. This dependency prompts the question of how to
387 proceed the DNN model in the absence of SONDE data at specific locations. As a
388 solution, we suggest employing morning temperature profiles from the European
389 Centre for Medium-Range Weather Forecasts' fifth-generation global reanalysis (ERA-
390 5, Hersbach et al., 2020) dataset when radiosonde data is not available to maintain the
391 model's operational integrity under sounding-data-constrained conditions. As one of the



392 most advanced reanalysis data, the ERA-5 is generated by the Integrated Forecasting
393 System coupled with a data assimilation system, and offer the meteorological data at a
394 spatial resolution of 0.25° - 0.25° .

395 Figure 10 assess the performance of DNN produced by multi-sources field
396 observations in estimating the PBLH by using morning temperature profiles from ERA-
397 5 (5 LT) and observed surface meteorological data. The temperature profiles in ERA-5
398 have a vertical resolution of 25-hPa in the lower atmosphere and are interpolated into
399 different levels described in Table 3. By utilizing ERA-5 morning profiles, the model
400 demonstrates similar performance to those results achieved with radiosonde inputs, as
401 evidenced by comparing Figure 10a and Figure 5. Moreover, this alternative approach
402 also shows enhanced accuracy over the native PBLH model outputs from ERA-5,
403 increasing the correlation coefficient from 0.74 to 0.86 and reducing the MAE from 0.3
404 km to 0.25 km. In addition, it is important to acknowledge that the PBLH represented
405 in ERA-5 is indicative of a grid-average value, approximately 25 km in scale, and
406 therefore inherently differs from site-specific data.

407 These findings highlight the alternative DNN model's robustness, offering a reliable
408 substitute for radiosonde data by leveraging reanalysis data with similar performance.
409 This demonstrates the DNN model's adaptability and potential as a practical tool for
410 PBLH estimation across various meteorological sites, especially in regions or periods
411 where radiosonde data may be lacking.

412 We further test the adaptability and generalizability of the DNN model, by applying
413 across different climatic and geographic regions. To this end, we extended our model



414 evaluation to include SONDE and surface meteorological data from the GoAmazon
415 (Tropical Rainforest) and CACTI (Middle Latitude Mountain) field campaigns.
416 Seasonality is accounted for as an input variable in the DNN model, with months in the
417 Southern Hemisphere adjusted to reflect their Northern Hemisphere seasonal
418 counterparts (e.g., July inputs are treated as January). The normalization process
419 (Section 3.1) was reapplied for the CACTI campaign data to adjust for notable pressure
420 level variations, ensuring input standardization with zero mean and unit variance.

421 Figure 11 presents the model's performance, in comparison to SONDE observations
422 for both GoAmazon and CACTI campaigns. The DNN model demonstrates
423 commendable adaptability, maintaining a strong correlation (0.86-0.88) with SONDE
424 measurements (Figure 11a-b). Further comparison is provided, which assess the
425 performance of ceilometer derived PBLH against SONDE for the same campaigns.
426 When assessing the performance of the ceilometer-derived PBLH against SONDE for
427 the same campaigns, the DNN model exhibited both stronger correlations and smaller
428 biases, as shown in Figure 11b-d.

429 Nevertheless, the analysis highlighted the presence of systematic biases, with
430 relatively larger MAE at the GoAmazon and CACTI sites compared to the SGP site.
431 Figure 12 underscores this by presenting a comparative analysis of PBLH means and
432 standard deviations across the three ARM sites. The early morning measurements
433 during 05-07 LT are excluded. The results, derived from SONDE, the DNN model,
434 ceilometer, and Doppler lidar data, reveal average differences in PBLH means relative
435 to SONDE. These differences suggest an overestimation (+15%) and underestimation



436 (-23%) by the DNN model for the GoAmazon and CACTI sites, respectively, compared
437 to the more consistent PBLH values at the SGP site.

438 The evident systematic deviations when applying the SGP-trained DNN model to
439 the diverse environments of GoAmazon and CACTI underscore the challenges in
440 generalizing the model to regions with significantly different meteorological
441 backgrounds. These findings point to the potential of DNN models for PBLH estimation
442 while also highlighting the necessity for region-specific model adjustments.

443

444 **5 Summary**

445 This study has developed a Multi-Structure DNN model for estimating PBLH using
446 conventional meteorological data. The DNN model is developed by leveraging a long-
447 term dataset of PBLH derived from radiosonde data and augmented with high-
448 resolution MPL and Doppler lidar observations. This model produced an PBLH dataset
449 over the SGP with robust accuracy, consistently yielding lower bias values across
450 various conditions and datasets. Utilizing conventional meteorological data, this
451 method generates a 27-year dataset over the SGP, encompassing periods with limited
452 remote sensing data availability. In situations where morning radiosonde data is
453 unavailable, ERA-5 data can be effectively employed to initiate the model, offering a
454 practical alternative.

455 An important aspect of this research involved comparing DNN models with diverse
456 remote sensing instruments. Although these instruments offer high temporal and
457 vertical resolution, discrepancies in PBLH estimation remain. Our DNN model,



458 leveraging a broad range of input features refined by their importance, constructs a
459 representation of PBL evolutions, frequently demonstrating a closer agreement with
460 SONDE-derived PBLH. In the absence of remote sensing data, the DNN model can
461 produce high-quality PBLH results from the conventional meteorology data.

462 The study has shown the DNN model's ability to synthesize complex patterns from
463 meteorological data, reflecting the versatility of machine learning in simulating the
464 boundary layer processes. Its application to varied geographic terrains and climates
465 during the GoAmazon and CACTI campaigns has further validated its adaptability,
466 demonstrating a high correlation between DNN-derived PBLH and SONDE-derived
467 PBLH. Nonetheless, systematic biases in regions outside the SGP highlight the
468 influence of regional factors in PBLH estimation and suggest the need for region-
469 specific refinements to the model.

470 In summary, this research introduces a machine learning framework for PBLH
471 estimation that is able to generate high-quality PBLH using meteorological data,
472 independent of remote sensing instruments. This methodology, alongside the datasets
473 derived from the deep learning model, is beneficial in advancing our understanding of
474 PBL daytime development including thermodynamics and dynamics. It also has
475 implications for improved representation of the PBL processes in weather forecasting
476 and climate models, particularly by offering the potential to diagnose PBL in models
477 through the integration of modeled meteorological data as input. Future efforts will be
478 directed towards refining this model to ensure its wide applicability over a global scale.



479 These developments aim to effectively tackle the challenges of systematic biases and
480 regional variability in PBLH estimation.

481

482 **Data Availability.** ARM radiosonde data, surface fluxes, and cloud masks are available
483 at https://adc.arm.gov/discovery/#/results/instrument_class_code::armbe. The datasets
484 of planetary boundary layer height used in this study can be downloaded from
485 https://adc.arm.gov/discovery/#/results/instrument_class_code::pblht. The DNN-
486 derived PBLH datasets over the SGP, CACTI, and GoAmazon are available at Zenodo
487 (<https://zenodo.org/records/10633811>) and will be uploaded to ARM data archive as a
488 product with detailed information upon acceptance.

489

490 **Author contributions.** TS conceptualized this study and carried out the analysis. TS
491 and YZ interpreted the data and wrote the manuscript. YZ supervised the project.

492

493 **Competing interests.** The contact author has declared that neither they nor their co-
494 authors have any competing interests.

495

496 **Acknowledgements:** We acknowledge the provision of radiosonde, lidar data, surface
497 meteorological data, and cloud products by the U.S. Department of Energy's ARM
498 program. Work at LLNL is performed under the auspices of the U.S. DOE by Lawrence
499 Livermore National Laboratory under Contract DE-AC52-07NA27344. This research
500 used resources of the National Energy Research Scientific Computing Center



501 (NERSC), a U.S. Department of Energy Office of Science User Facility located at
502 Lawrence Berkeley National Laboratory, operated under Contract No. DE-AC02-
503 05CH11231.

504

505 **Financial support.** This work is supported by the DOE Atmospheric System Research
506 (ASR) Science Focus Area (SFA) THREAD project.

507

508 **References**

- 509 Abadi, M., Agarwal, A., Barham, P., Brevdo, E., Chen, Z., Citro, C., Corrado, G.S.,
510 Davis, A., Dean, J., Devin, M. and Ghemawat, S., 2016. Tensorflow: Large-scale
511 machine learning on heterogeneous distributed systems. arXiv preprint
512 arXiv:1603.04467.
- 513 Altmann, A., Tološi, L., Sander, O. and Lengauer, T., 2010. Permutation importance:
514 a corrected feature importance measure. *Bioinformatics*, 26(10), pp.1340-1347.
- 515 Barlow, J.F., Dunbar, T.M., Nemitz, E.G., Wood, C.R., Gallagher, M.W., Davies, F.,
516 O'Connor, E. and Harrison, R.M., 2011. Boundary layer dynamics over London,
517 UK, as observed using Doppler lidar during REPARTEE-II. *Atmospheric*
518 *Chemistry and Physics*, 11(5), pp.2111-2125.
- 519 Battaglia, P.W., Hamrick, J.B., Bapst, V., Sanchez-Gonzalez, A., Zambaldi, V.,
520 Malinowski, M., Tacchetti, A., Raposo, D., Santoro, A., Faulkner, R. and
521 Gulcehre, C., 2018. Relational inductive biases, deep learning, and graph
522 networks. arXiv preprint arXiv:1806.01261.
- 523 Beamesderfer, E.R., Buechner, C., Faiola, C., Helbig, M., Sanchez-Mejia, Z.M.,
524 Yáñez-Serrano, A.M., Zhang, Y. and Richardson, A.D., 2022. Advancing cross-
525 disciplinary understanding of land-atmosphere interactions. *Journal of*
526 *Geophysical Research: Biogeosciences*, 127(2), p.e2021JG006707.
- 527 Cadeddu, M. P., Turner, D. D., and Liljegren, J. C., 2009. A neural network for real-
528 time retrievals of PWV and LWP from Arctic millimeter-wave ground-based
529 observations, *IEEE T. Geosci. Remote*, 47, 1887–1900.
- 530 Caughey, S.J. (1984). Observed characteristics of the atmospheric boundary layer. In
531 *Atmospheric turbulence and air pollution modelling* (pp. 107-158). Springer,
532 Dordrecht.
- 533 Chu, Y., Li, J., Li, C., Tan, W., Su, T. and Li, J. (2019). Seasonal and diurnal
534 variability of planetary boundary layer height in Beijing: Intercomparison between
535 MPL and WRF results. *Atmospheric research*, 227, pp.1-13.



- 536 Chu, Y., Li, J., Li, C., Tan, W., Su, T. and Li, J., 2019. Seasonal and diurnal
537 variability of planetary boundary layer height in Beijing: Intercomparison between
538 MPL and WRF results. *Atmospheric research*, 227, pp.1-13.
- 539 Clothiaux, E. E., Ackerman, T. P., Mace, G. G., Moran, K. P., Marchand, R. T.,
540 Miller, M. A., and Martner, B. E. (2000): Objective determination of cloud heights
541 and radar reflectivities using a combination of active remote sensors at the ARM
542 CART sites. *J. Appl. Meteorol.*, 39(5), 645–665.
- 543 Clothiaux, E.E., Miller, M.A., Perez, R.C., Turner, D.D., Moran, K.P., Martner, B.E.,
544 Ackerman, T.P., Mace, G.G., Marchand, R.T., Widener, K.B. and Rodriguez, D.J.
545 (2001). The ARM millimeter wave cloud radars (MMCRs) and the active remote
546 sensing of clouds (ARSCL) value added product (VAP) (No. DOE/SC-
547 ARM/VAP-002.1). DOE Office of Science Atmospheric Radiation Measurement
548 (ARM) Program (United States).
- 549 Cohn, S. A. and Angevine, W. M. (2000). Boundary layer height and entrainment
550 zone thickness measured by lidars and wind-profiling radars, *J. Appl. Meteorol.*,
551 39, 1233–1247.
- 552 Cook, D.R. (2018). Energy balance bowen ratio station (EBBR) instrument handbook
553 (No. DOE/SC-ARM/TR-037). DOE Office of Science Atmospheric Radiation
554 Measurement (ARM) Program (United States).
- 555 Date, Y. and Kikuchi, J., 2018. Application of a deep neural network to metabolomics
556 studies and its performance in determining important variables. *Analytical*
557 *chemistry*, 90(3), pp.1805-1810.
- 558 Davis, K.J., Gamage, N., Hagelberg, C.R., Kiemle, C., Lenschow, D.H., & Sullivan,
559 P.P. (2000). An objective method for deriving atmospheric structure from airborne
560 lidar observations. *Journal of Atmospheric and Oceanic Technology*, 17, 1455-
561 1468
- 562 Emanuel, K.A. (1994). *Atmospheric convection.*: Oxford University Press on Demand
- 563 Ferrare, Richard. Raman lidar/AERI PBL Height Product. United States: N. p., 2012.
564 Web. doi:10.5439/1169501.
- 565 Gagne II, D. J., Haupt, S. E., Nychka, D. W., and Thompson, G.: Interpretable deep
566 learning for spatial analysis of severe hailstorms, *Mon. Weather Rev.*, 147, 2827–
567 2845, (2019).
- 568 Ganaie, M.A., Hu, M., Malik, A.K., Tanveer, M. and Suganthan, P.N., 2022.
569 Ensemble deep learning: A review. *Engineering Applications of Artificial*
570 *Intelligence*, 115, p.105151.
- 571 Garratt, J. R. (1994): The atmospheric boundary layer. *Earth-Sci. Rev.*, 37(1–2), 89–
572 134.
- 573 Guo, J., Su, T., Li, Z., Miao, Y., Li, J., Liu, H., Xu, H., Cribb, M. and Zhai, P. (2017).
574 Declining frequency of summertime local-scale precipitation over eastern China
575 from 1970 to 2010 and its potential link to aerosols. *Geophysical Research*
576 *Letters*, 44(11), pp.5700-5708.
- 577 Guo, J., Zhang, J., Shao, J., Chen, T., Bai, K., Sun, Y., Li, N., Wu, J., Li, R., Li, J. and
578 Guo, Q., 2024. A merged continental planetary boundary layer height dataset



- 579 based on high-resolution radiosonde measurements, ERA5 reanalysis, and
580 GLDAS. *Earth System Science Data*, 16(1), pp.1-14.
- 581 Guo, J., Zhang, J., Yang, K., Liao, H., Zhang, S., Huang, K., Lv, Y., Shao, J., Yu, T.,
582 Tong, B. and Li, J., 2021. Investigation of near-global daytime boundary layer
583 height using high-resolution radiosondes: first results and comparison with ERA5,
584 MERRA-2, JRA-55, and NCEP-2 reanalyses. *Atmospheric Chemistry and
585 Physics*, 21(22), pp.17079-17097.
- 586 Helbig, M., Gerken, T., Beamesderfer, E.R., Baldocchi, D.D., Banerjee, T., Biraud,
587 S.C., Brown, W.O., Brunsell, N.A., Burakowski, E.A., Burns, S.P. and
588 Butterworth, B.J., 2021. Integrating continuous atmospheric boundary layer and
589 tower-based flux measurements to advance understanding of land-atmosphere
590 interactions. *Agricultural and Forest Meteorology*, 307, p.108509.
- 591 Hersbach, H., Bell, B., Berrisford, P., Hirahara, S., Horányi, A., Muñoz-Sabater, J.,
592 Nicolas, J., Peubey, C., Radu, R., Schepers, D. and Simmons, A., 2020. The
593 ERA5 global reanalysis. *Quarterly Journal of the Royal Meteorological Society*,
594 146(730), pp.1999-2049.
- 595 Holdridge, D., Ritsche, M., Prell, J., and Coulter, R. (2011): Balloon-borne sounding
596 system (SONDE) handbook, <https://www.arm.gov/capabilities/instruments/sonde>.
- 597 Holtzlag, A.A. and Nieuwstadt, F.T. (1986). Scaling the atmospheric boundary layer.
598 *Boundary-Layer Meteorology*, 36(1-2), pp.201-209.
- 599 Holzworth, G. C. (1964). Estimates of mean maximum mixing depths in the
600 contiguous United States. *Monthly Weather Review*, 92(5), 235–242.
601 [https://doi.org/10.1175/1520-0493\(1964\)092<0235:EOMMMD>2.3.CO;2](https://doi.org/10.1175/1520-0493(1964)092<0235:EOMMMD>2.3.CO;2)
- 602 Kaimal, J.C. and Finnigan, J.J. (1994). *Atmospheric boundary layer flows: their
603 structure and measurement*. Oxford university press.
- 604 Kollias, P., Bharadwaj, N., Clothiaux, E.E., Lamer, K., Oue, M., Hardin, J., Isom, B.,
605 Lindenmaier, I., Matthews, A., Luke, E.P. and Giangrande, S.E. (2020). The ARM
606 radar network: At the leading edge of cloud and precipitation observations.
607 *Bulletin of the American Meteorological Society*, 101(5), pp.E588-E607.
- 608 Kotthaus, S., Bravo-Aranda, J.A., Collaud Coen, M., Guerrero-Rascado, J.L., Costa,
609 M.J., Cimini, D., O'Connor, E.J., Hervo, M., Alados-Arboledas, L., Jiménez-
610 Portaz, M. and Mona, L., 2023. Atmospheric boundary layer height from ground-
611 based remote sensing: a review of capabilities and limitations. *Atmospheric
612 Measurement Techniques*, 16(2), pp.433-479.
- 613 Krishnamurthy, R., Newsom, R.K., Berg, L.K., Xiao, H., Ma, P.L. and Turner, D.D.,
614 2021. On the estimation of boundary layer heights: a machine learning approach.
615 *Atmospheric Measurement Techniques*, 14(6), pp.4403-4424.
- 616 Lareau, N.P., Zhang, Y. and Klein, S.A., 2018. Observed boundary layer controls on
617 shallow cumulus at the ARM Southern Great Plains site. *Journal of the
618 Atmospheric Sciences*, 75(7), pp.2235-2255.
- 619 Li, H., Liu, B., Ma, X., Jin, S., Wang, W., Fan, R., Ma, Y., Wei, R. and Gong, W.,
620 2023. Estimation of Planetary Boundary Layer Height from Lidar by Combining
621 Gradient Method and Machine Learning Algorithms. *IEEE Transactions on
622 Geoscience and Remote Sensing*.



- 623 Li, Z., Guo, J., Ding, A., Liao, H., Liu, J., Sun, Y., Wang, T., Xue, H., Zhang, H. and
624 Zhu, B., 2017. Aerosol and boundary-layer interactions and impact on air quality.
625 National Science Review, 4(6), pp.810-833.
- 626 Lilly, D.K. (1968). Models of Cloud-Topped Mixed Layers under a Strong Inversion.
627 Quarterly Journal of the Royal Meteorological Society, 94, 292-&
628 Liu, F., Page, A., Strode, S. A., Yoshida, Y., Choi, S., Zheng, B., Lamsal, L. N., Li,
629 C., Krotkov, N. A., Eskes, H., and Veefkind, P. (2020). Abrupt decline in
630 tropospheric nitrogen dioxide over China after the outbreak of COVID-19.
631 Science Advances, 6(28), eabc2992
- 632 Liu, L., Jiang, H., He, P., Chen, W., Liu, X., Gao, J. and Han, J., 2019. On the
633 variance of the adaptive learning rate and beyond. arXiv preprint
634 arXiv:1908.03265. Garratt, J.R. (1994). The atmospheric boundary layer. Earth-
635 Science Reviews, 37(1-2), pp.89-134.
- 636 Liu, S. and Liang, X.Z., 2010. Observed diurnal cycle climatology of planetary
637 boundary layer height. Journal of Climate, 23(21), pp.5790-5809.
- 638 Liu, Z., Chang, J., Li, H., Chen, S. and Dai, T., 2022. Estimating boundary layer
639 height from lidar data under complex atmospheric conditions using machine
640 learning. Remote Sensing, 14(2), p.418.
- 641 Liu, Z., Chang, J., Li, H., Chen, S. and Dai, T., 2022. Estimating boundary layer
642 height from lidar data under complex atmospheric conditions using machine
643 learning. Remote Sensing, 14(2), p.418.
- 644 Mahrt, L. (1999). Stratified atmospheric boundary layers. Boundary-Layer
645 Meteorology, 90(3), pp.375-396.
- 646 Matsui, T., Masunaga, H., Pielke, R.A., & Tao, W.K. (2004). Impact of aerosols and
647 atmospheric thermodynamics on cloud properties within the climate system.
648 Geophysical Research Letters, 31
- 649 McGovern, A., Elmore, K. L., Gagne, D. J., Haupt, S. E., Karstens, C. D., Lagerquist,
650 R., Smith, T., and Williams, J. K.: Using artificial intelligence to improve real-
651 time decision-making for high-impact weather, B. Am. Meteorol. Soc., 98, 2073–
652 2090, (2017).
- 653 Melfi, S.H., Spinhirne, J.D., Chou, S.H. and Palm, S.P. (1985). Lidar observations of
654 vertically organized convection in the planetary boundary layer over the ocean.
655 Journal of climate and applied meteorology, 24(8), pp.806-821.
- 656 Menut, L., Flamant, C., Pelon, J., & Flamant, P.H. (1999). Urban boundary-layer
657 height determination from lidar measurements over the Paris area. Applied Optics,
658 38, 945-954
- 659 Molero, F., Barragán, R. and Artíñano, B., 2022. Estimation of the atmospheric
660 boundary layer height by means of machine learning techniques using ground-
661 level meteorological data. Atmospheric Research, 279, p.106401.
- 662 Nielsen, M.A., 2015. Neural networks and deep learning (Vol. 25, pp. 15-24). San
663 Francisco, CA, USA: Determination press.
- 664 Pang, B., Nijkamp, E. and Wu, Y.N., 2020. Deep learning with tensorflow: A review.
665 Journal of Educational and Behavioral Statistics, 45(2), pp.227-248.



- 666 Park, O.H., Seo, S.J., & Lee, S.H. (2001). Laboratory simulation of vertical plume
667 dispersion within a convective boundary layer - Research note. *Boundary-Layer*
668 *Meteorology*, 99, 159-169
- 669 Raju, V.G., Lakshmi, K.P., Jain, V.M., Kalidindi, A. and Padma, V., 2020, August.
670 Study the influence of normalization/transformation process on the accuracy of
671 supervised classification. In *2020 Third International Conference on Smart*
672 *Systems and Inventive Technology (ICSSIT)* (pp. 729-735). IEEE.
- 673 Rieutord, T., Aubert, S. and Machado, T., 2021. Deriving boundary layer height from
674 aerosol lidar using machine learning: KABL and ADABL algorithms.
675 *Atmospheric Measurement Techniques*, 14(6), pp.4335-4353.
- 676 Sawyer, V. and Li, Z., 2013. Detection, variations and intercomparison of the
677 planetary boundary layer depth from radiosonde, lidar and infrared spectrometer.
678 *Atmospheric environment*, 79, pp.518-528.
- 679 Schmidhuber, J., 2015. Deep learning in neural networks: An overview. *Neural*
680 *networks*, 61, pp.85-117.
- 681 Seidel, D.J., Ao, C.O. and Li, K., 2010. Estimating climatological planetary boundary
682 layer heights from radiosonde observations: Comparison of methods and
683 uncertainty analysis. *Journal of Geophysical Research: Atmospheres*, 115(D16).
- 684 Sivaraman, Chitra, and Zhang, Damao. Planetary Boundary Layer Height derived
685 from Doppler Lidar (DL) data. United States: N. p., 2021. Web.
686 doi:10.5439/1726254.
- 687 Sleeman, J., Halem, M., Yang, Z., Caicedo, V., Demoz, B. and Delgado, R., 2020,
688 September. A deep machine learning approach for lidar based boundary layer
689 height detection. In *IGARSS 2020-2020 IEEE international geoscience and*
690 *remote sensing symposium* (pp. 3676-3679). IEEE.
- 691 Stull, R.B. (1988). *An Introduction to Boundary Layer Meteorology*. Dordrecht:
692 Springer Netherlands
- 693 Su, T., Li, J., Li, C., Xiang, P., Lau, A.K.H., Guo, J., Yang, D. and Miao, Y., 2017.
694 An intercomparison of long-term planetary boundary layer heights retrieved from
695 CALIPSO, ground-based lidar, and radiosonde measurements over Hong Kong.
696 *Journal of Geophysical Research: Atmospheres*, 122(7), pp.3929-3943.
- 697 Su, T., Li, Z. and Zheng, Y. (2023). Cloud-Surface Coupling Alters the Morning
698 Transition From Stable to Unstable Boundary Layer. *Geophysical Research*
699 *Letters*, 50(5), p.e2022GL102256.
- 700 Su, T., Li, Z., and Kahn, R. (2020): A new method to retrieve the diurnal variability of
701 planetary boundary layer height from lidar under different thermodynamic
702 stability conditions. *Remote Sens. Environ.*, 237, 111519.
- 703 Su, T., Li, Z., Zheng, Y., Wu, T., Wu, H. and Guo, J., (2022a). Aerosol-boundary
704 layer interaction modulated entrainment process. *NPJ Climate and Atmospheric*
705 *Science*, 5(1), p.64.
- 706 Su, T., Zheng, Y. and Li, Z., (2022b). Methodology to determine the coupling of
707 continental clouds with surface and boundary layer height under cloudy conditions
708 from lidar and meteorological data. *Atmospheric Chemistry and Physics*, 22(2),
709 pp.1453-1466.



- 710 Summa, D., Di Girolamo, P., Stelitano, D. and Cacciani, M., 2013. Characterization
711 of the planetary boundary layer height and structure by Raman lidar: comparison
712 of different approaches. *Atmospheric Measurement Techniques*, 6(12), pp.3515-
713 3525.
- 714 Sze, V., Chen, Y.H., Yang, T.J. and Emer, J.S., 2017. Efficient processing of deep
715 neural networks: A tutorial and survey. *Proceedings of the IEEE*, 105(12),
716 pp.2295-2329.
- 717 Tang, S., Xie, S., Zhang, M., Tang, Q., Zhang, Y., Klein, S. A., Cook, D. R., and
718 Sullivan, R. C. (2019): Differences in eddy-correlation and energy-balance surface
719 turbulent heat flux measurements and their impacts on the large-scale forcing
720 fields at the ARM SGP site. *J. Geophys. Res. Atmos.*, 124, 3301–3318,
721 doi.org/10.1029/2018JD029689.
- 722 Tucker, S.C., Brewer, W.A., Banta, R.M., Senff, C.J., Sandberg, S.P., Law, D.C.,
723 Weickmann, A.M., & Hardesty, R.M. (2009). Doppler Lidar Estimation of Mixing
724 Height Using Turbulence, Shear, and Aerosol Profiles. *Journal of Atmospheric
725 and Oceanic Technology*, 26, 673-688
- 726 Vassallo, D., Krishnamurthy, R., and Fernando, H. J. S.: Decreasing wind speed
727 extrapolation error via domain-specific feature extraction and selection, *Wind
728 Energ. Sci.*, 5, 959–975, <https://doi.org/10.5194/wes-5-959-2020>, 2020.
- 729 Wesely, M. L., Cook, D. R., and Coulter, R. L. (1995): Surface heat flux data from
730 energy balance Bowen ratio systems (No. ANL/ER/CP-84065; CONF-9503104-
731 2). Argonne National Lab., IL (United States).
- 732 Xie, S., McCoy, R. B., Klein, S. A., Cederwall, R. T., Wiscombe, W. J., Jensen, M.
733 P., Johnson, K. L., Clothiaux, E. E., Gaustad, K. L., Long, C. N., and Mather, J.
734 H. (2010): Clouds and more: ARM climate modeling best estimate data: a new
735 data product for climate studies. *Bull. Amer. Meteorol. Soc.*, 91(1), 13–20.
- 736 Ye, J., Liu, L., Wang, Q., Hu, S. and Li, S., 2021. A novel machine learning algorithm
737 for planetary boundary layer height estimation using AERI measurement data.
738 *IEEE Geoscience and Remote Sensing Letters*, 19, pp.1-5.
- 739 Zhang, D., Comstock, J. and Morris, V., (2022). Comparison of planetary boundary
740 layer height from ceilometer with ARM radiosonde data. *Atmospheric
741 Measurement Techniques*, 15(16), pp.4735-4749.
- 742 Zhang, Z., (2018), June. Improved adam optimizer for deep neural networks. In 2018
743 IEEE/ACM 26th international symposium on quality of service (IWQoS) (pp. 1-
744 2). IEEE.



745 **Table list:**

746 **Table 1.** This table lists the varying structures of hidden layers used by each ensemble
747 member for PBLH estimation. Each configuration is expressed as an array, with the
748 number of elements indicating the number of layers and each value specifying the
749 number of neurons activated in the corresponding layer. For instance, a structure
750 denoted as [52, 28, 16] comprises three hidden layers containing 52, 28, and 16 neurons,
751 respectively.

752

Ensemble Member	Different Structures in Hidden Layer	Ensemble Member	Different Structures in Hidden Layer
Member 1	[52, 28, 16]	Member 6	[57, 44, 19]
Member 2	[61, 43, 20]	Member 7	[55, 43, 19]
Member 3	[59, 45, 19]	Member 8	[57, 43, 15]
Member 4	[60, 45, 23]	Member 9	[59, 41, 20, 10]
Member 5	[57, 45, 23]	Member 10	[57, 43, 18, 9]

753

754

755

756

757

758

759

760

761

762

763

764

765



766 **Table 2.** Distribution of Dataset Samples for deep learning neural network (DNN)
767 Training and Validation. This table details the sample data in different local time used
768 for the development and validation of DNN to estimate planetary boundary layer height
769 (PBLH). The first column lists the available PBLH derived from radiosonde (SONDE,
770 Liu and Liang, 2010) during various local hours from 1994 to 2016. The second column
771 supplements the dataset with a combined MPL and SONDE approach (Su et al. 2020)
772 and Doppler Lidar-derived PBLH (Sivaraman and Zhang, 2021) used in the absence of
773 SONDE measurements. Seventy percent of the combined dataset from the first and
774 second columns was randomly selected for the model's training. The third column
775 provides the number of SONDE measurements available for validation purposes. Since
776 morning SONDE serves as the input and boundary condition.

Local Time (h)	SONDE	Supplement Lidar Dataset	SONDE for Validation
5	7163	0	0
6	22	1181	0
7	3	1186	0
8	1225	2541	453
9	16	2629	8
10	9	2732	3
11	6513	13	3307
12	26	2797	9
13	14	2694	47
14	2131	2334	728
15	28	2555	9
16	3	2730	1
17	6503	2	3348



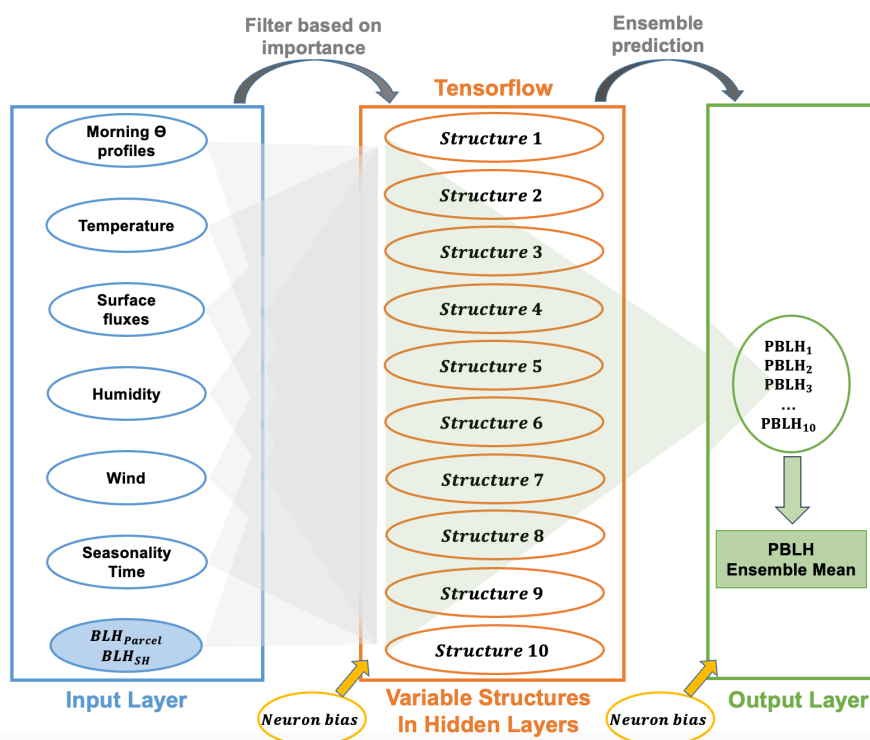
777 **Table 3.** Feature Importance in the Deep Learning Model. This table presents the
 778 importance scores of each input feature used in the deep learning model to estimate the
 779 planetary boundary layer height. The features include local time, month, relative
 780 humidity, U and V wind components, surface pressure, precipitation, temperature,
 781 lifting condensation level (LCL), boundary layer height derived from sensible heat and
 782 parcel methods (Sensible Heat BLH and Parcel Method BLH), sensible and latent heat,
 783 and profiles of potential temperature (θ) at different heights. The importance scores
 784 quantify the relative contribution of each feature to the model's predictive accuracy.

Feature	Importance	Feature	Importance
Local Time	0.001553446	θ 0.45km	0.002378
Month	0.01447574	θ 0.5km	0.002168
RH (i-1)	0.006151263	θ 0.55km	0.002156
RH (i)	0.065531985	θ 0.6km	0.00223
U Wind (i-1)	0.001555849	θ 0.65km	0.001738
U Wind (i)	0.008374529	θ 0.7km	0.001382
V Wind (i-1)	0.010233951	θ 0.75km	0.001251
V Wind (i)	0.009699108	θ 0.8km	0.001533
Surface Pressure (i-1)	0.000757657	θ 0.85km	0.001889
Surface Pressure (i)	0.004098737	θ 0.9km	0.001667
Rain Rate (i-1)	0.000313072	θ 0.95km	0.001062
Rain Rate (i)	0.000442731	θ 1km	0.000533
Temperature (i-1)	0.004147774	θ 1.1km	0.000657
Temperature (i)	0.005575494	θ 1.2km	0.000172
LCL (i-1)	0.001331462	θ 1.3km	-8.3E-05
LCL (i)	0.011779424	θ 1.4km	-0.00047
Sensible Heat BLH (i-1)	0.004322382	θ 1.5km	-8.1E-05
Sensible Heat BLH (i)	0.01068823	θ 1.6km	0.000436
Parcel Method BLH (i-1)	0.035470469	θ 1.7km	0.000855
Parcel Method BLH (i)	0.089339075	θ 1.8km	0.000374
Sensible Heat (i-1)	0.00440638	θ 1.9km	0.000542
Sensible Heat (i)	0.00138861	θ 2km	0.00044
Latent Heat (i-1)	0.005000932	θ 2.2km	-0.00044
Latent Heat (i)	0.006878718	θ 2.4km	-0.00088
θ 0.05km	0.054674179	θ 2.6km	-0.00072
θ 0.1km	0.004824675	θ 2.8km	0.000325
θ 0.15km	0.000101218	θ 3km	0.001006
θ 0.2km	0.000781841	θ 3.2km	0.000577
θ 0.25km	0.001795084	θ 3.4km	0.000799
θ 0.3km	0.002307328	θ 3.6km	0.00064
θ 0.35km	0.003030368	θ 3.8km	0.000747
θ 0.4km	0.00309969	θ 4km	0.004221



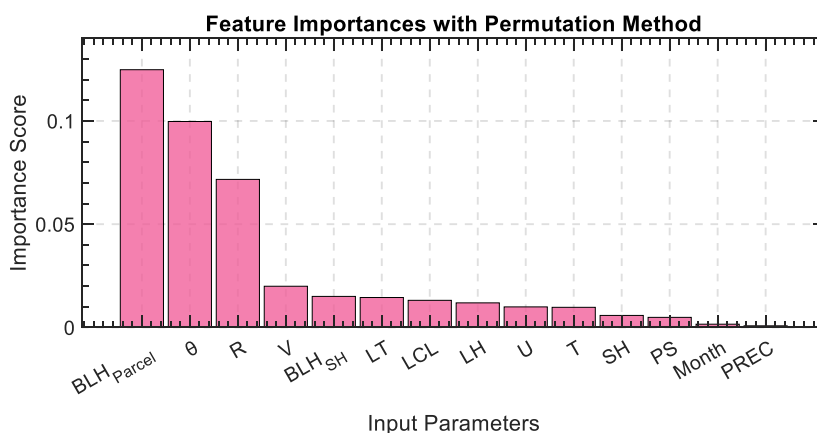
785 **Figures**

Deep Neural Networks for estimating boundary layer height



786

787 **Figure 1.** Schematic of the multi-structure deep neural networks (DNN) used for
788 estimating the planetary boundary layer height (PBLH). Input features, including
789 morning potential temperature profiles, temperature, wind, humidity, surface fluxes,
790 seasonality, and time, are filtered based on importance and fed into the network. The
791 system comprises ten distinct hidden layer structures, each processing the inputs to
792 model PBLH. The outputs from these structures are then synthesized to determine the
793 final PBLH value, leveraging the diverse representations of atmospheric dynamics
794 captured by each neural network configuration. Neuron biases are applied at the output
795 and hidden layers to fine-tune the model's performance.



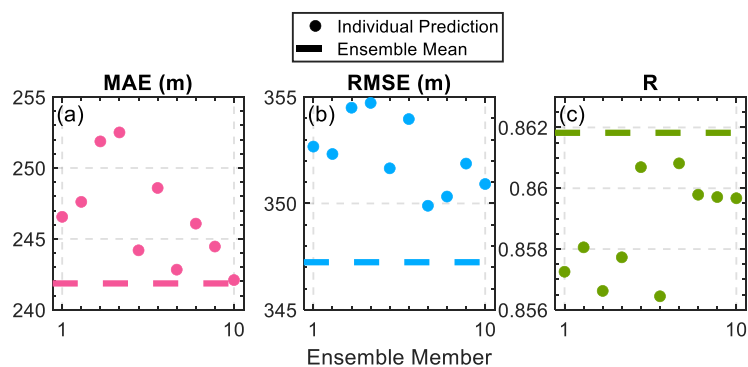
796

797 **Figure 2.** Feature importance with permutation method in the deep learning model.

798 This table presents the importance scores of each input feature used in the deep learning
799 model to estimate the PBLH. The features include local time (LT), month, relative
800 humidity (R), surface U and V wind components, pressure at the surface (PS),
801 precipitation (PREC), surface temperature (T), sensible and latent heat (SH and LH),
802 surface-derived lifting condensation level (LCL), boundary layer height derived from
803 sensible heat and parcel methods (BLH_{parcel} and BLH_{SH}), and profiles of potential
804 temperature (θ). The importance scores quantify the relative contribution of each
805 feature to the model's predictive accuracy.

806

807



808

809 **Figure 3:** Performance metrics of individual ensemble members and the ensemble
810 mean in estimating planetary boundary layer height (PBLH). Panel (a) displays the
811 mean absolute error (MAE), panel (b) the root mean square error (RMSE), and panel
812 (c) the correlation coefficient (R) for each of the ten ensemble members (represented
813 by dots) and the ensemble mean (indicated by the horizontal dash line). The ensemble
814 approach demonstrates improved accuracy and reliability in PBLH estimation as
815 evidenced by the aggregation of individual model predictions into a robust ensemble
816 mean.

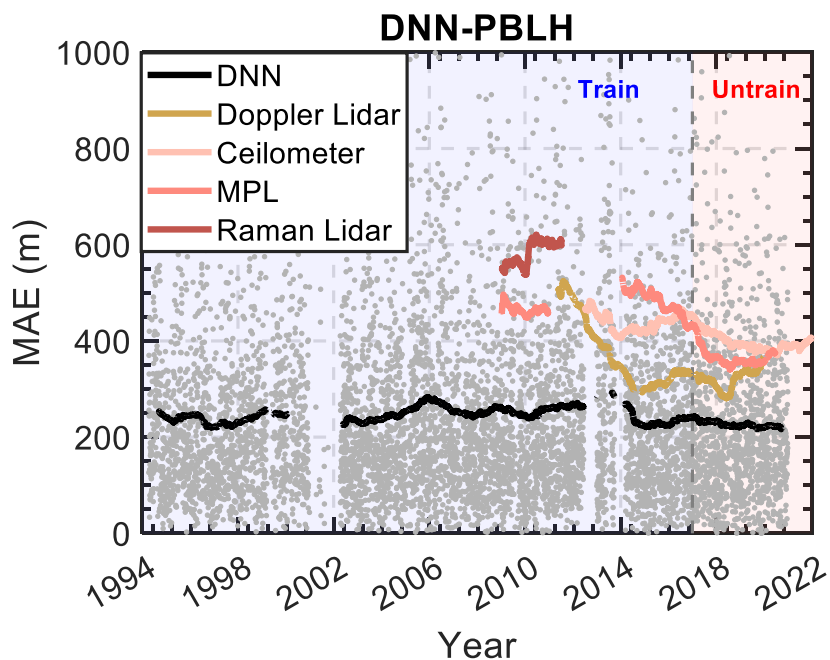
817

818

819

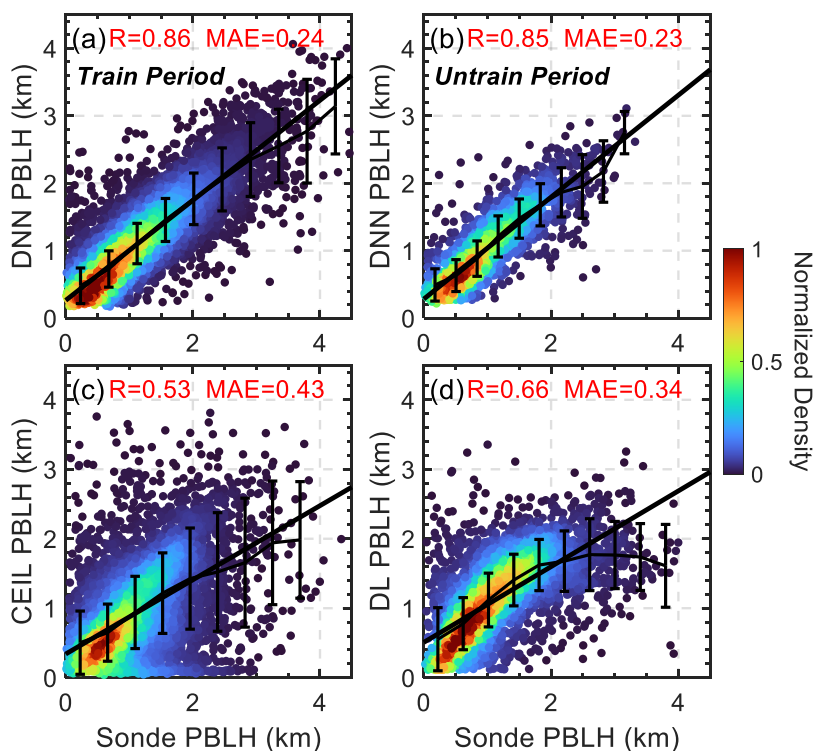
820

821



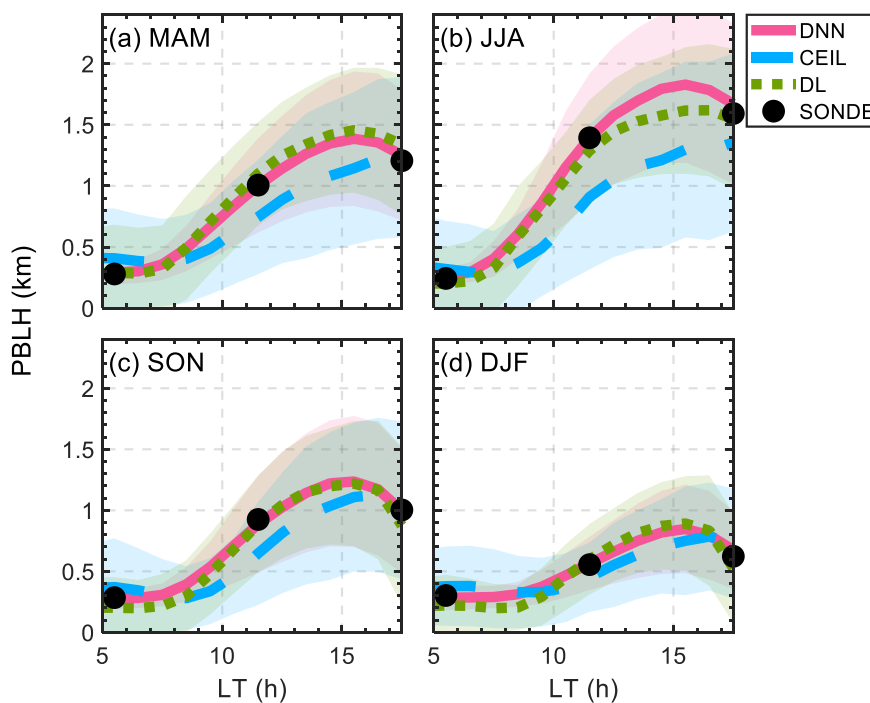
822

823 **Figure 4:** Comparative analysis of the mean absolute error (MAE) in PBLH estimation
824 using different methodologies. PBLH derived from SONDE is considered as the ground
825 truth. The DNN approach is shown in black, doppler lidar (Sivaraman and Zhang, 2021)
826 in yellow, ceilometer (Zhang et al. 2022) in pink, micro-pulse lidar (MPL, Sawyer and
827 Li, 2013) in light red, and Raman lidar (Ferrare, 2012) in dark red. DNN model is
828 trained during 1994-2016. Individual MAE values for DNN are represented by gray
829 dots, while the solid lines denote the smoothed MAE for each method with a 2-year
830 smooth window.



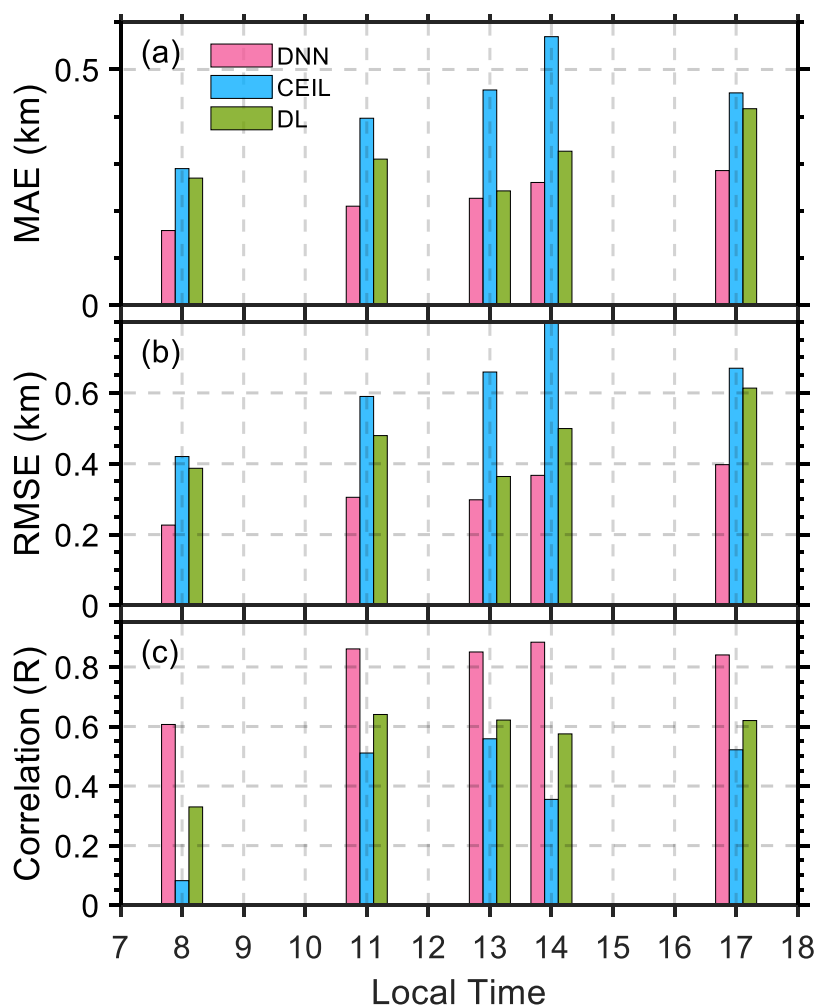
831

832 **Figure 5:** Scatter plots comparing observed radiosonde (SONDE) PBLH with estimates
833 from the machine learning model and lidar observations. Panels (a) and (b) show the
834 PBLH estimated by the deep neural network (DNN) during the trained period (1994-
835 2016) and the untrained period (2017-2020), respectively, with corresponding
836 correlation coefficients (R) and mean absolute errors (MAE). Panels (c) and (d) display
837 comparisons of Sonde PBLH with ceilometer (CEIL) and doppler lidar (DL) derived
838 PBLH, respectively. The color gradient indicates the normalized density of data points,
839 while the solid black line represents the line of best fit and error bars indicates the mean
840 and standard deviations for each bin.



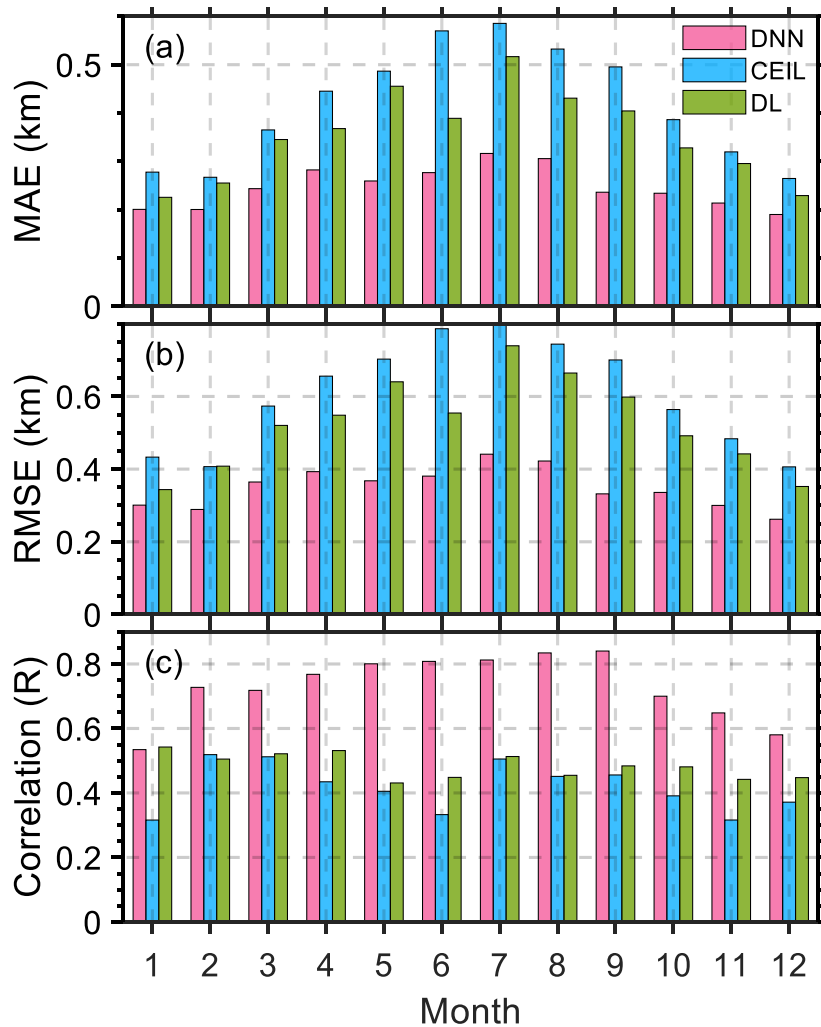
841

842 **Figure 6:** Seasonal-averaged daytime evolution of planetary boundary layer height
843 (PBLH) derived from various methods. The panels represent the mean PBLH values
844 throughout the day for different seasons: (a) March-April-May (MAM), (b) June-July-
845 August (JJA), (c) September-October-November (SON), and (d) December-January-
846 February (DJF). The PBLH values estimated by the deep neural network (DNN) are
847 shown in red, ceilometer (CEIL) estimates in blue, Doppler lidar (DL) in green, and
848 observed radiosonde (SONDE) data in black. Shaded areas around the lines indicate the
849 standard deviations within each method.



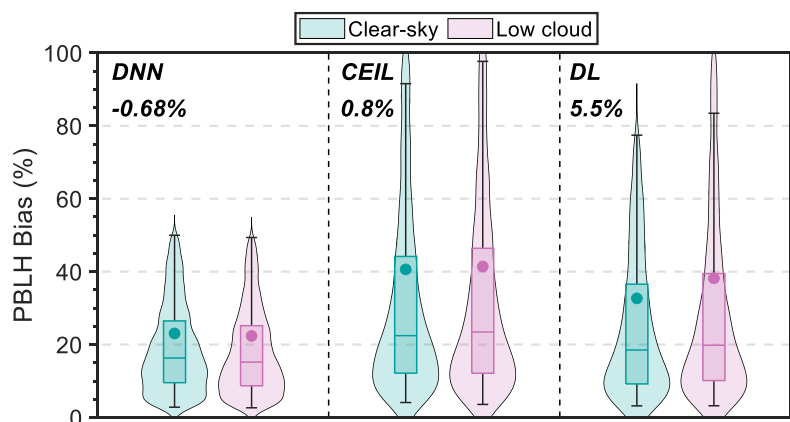
850

851 **Figure 7:** Diurnal variations in the performance metrics for estimating PBLH using
852 different datasets. (a) Shows the correlation coefficient (R), (b) represents the root mean
853 square error (RMSE), and (c) depicts the mean absolute error (MAE) at various local
854 times throughout the day. The deep learning neural network (DNN) estimates are in
855 blue, ceilometer (CEIL) derived estimates are in pink, and doppler lidar (DL) estimates
856 are in green. Note that these biases metrics are calculated using SONDE PBLH as the
857 standard. The availability of SONDE data for different hours is detailed in Table 2.



858

859 **Figure 8:** Similar to Figure 7, but for MAE, RMSE, and R for different month.

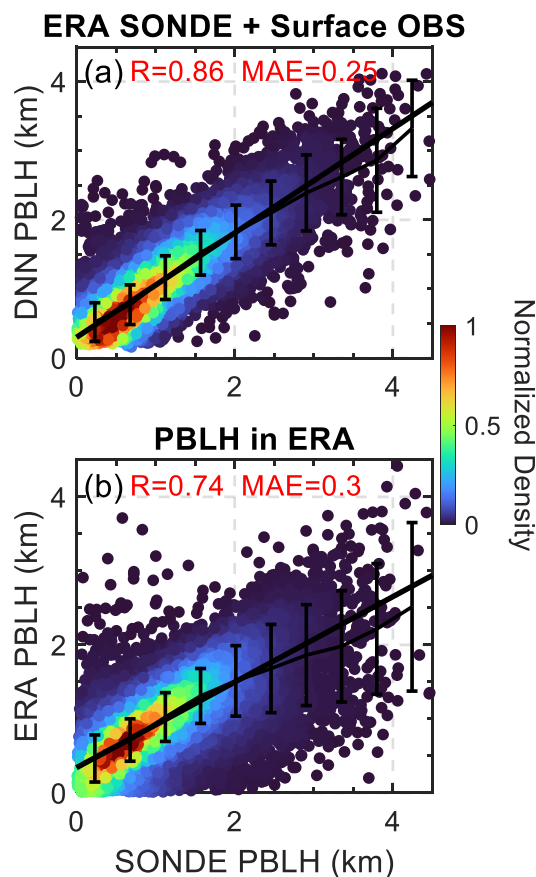


860

861 **Figure 9:** Comparative analysis of PBLH estimation bias under clear-sky and low cloud
862 conditions for various methods. Bias percentages are computed as the absolute bias
863 normalized by the mean PBLH for each condition, with the number above each method
864 indicating the difference in bias between low cloud and clear-sky scenarios. The
865 boxplots detail the 10th, 25th, 50th, 75th, and 90th percentiles, while shaded areas in
866 violin plots illustrate the distribution of dataset biases. The dots indicate the mean value
867 for each condition.

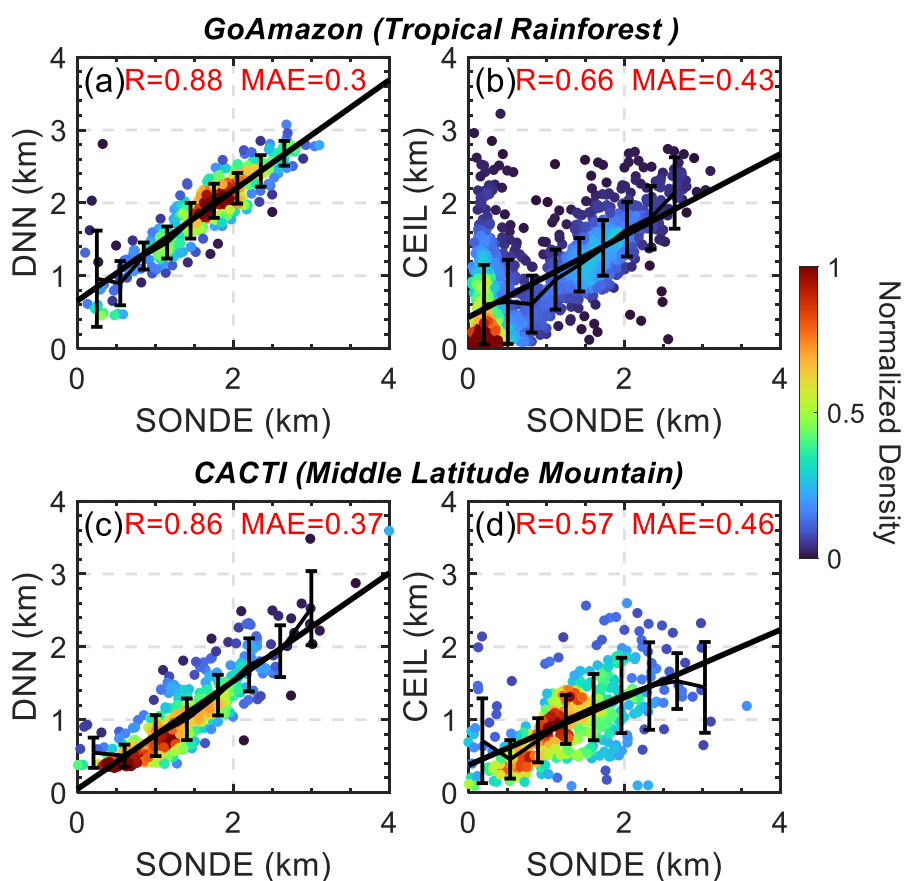
868

869



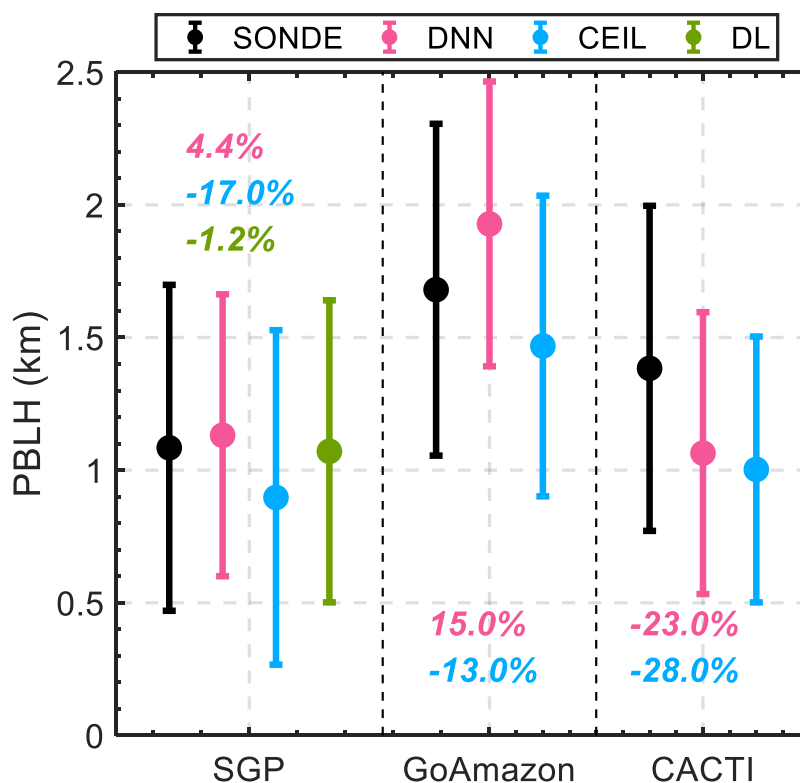
870

871 **Figure 10:** Scatter plots comparing SONDE PBLH with estimates from the DNN and
872 ERA-5. (a) The comparison between observed SONDE PBLH and estimates from the
873 DNN model, which utilizes morning temperature profiles (5 LT) from ERA-5 (ERA
874 Profile) and observed surface meteorological data (surface OBS) as inputs. (b) The
875 correlation comparison observed SONDE PBLH and PBLH model outputs from the
876 ERA-5 datasets. The color gradient in both panels represents the normalized density of
877 data points, while the solid black line indicates the linear regression, and the error bars
878 denote the mean and standard deviations for each bin.



879

880 **Figure 11:** Validation of the DNN trained over the SGP for the GoAmazon (Tropical
881 Rainforest) and CACTI (Middle Latitude Mountain) field campaigns. Panels (a) and (c)
882 illustrate the correlation (R) and mean absolute error (MAE) between DNN predictions
883 and SONDE observations for GoAmazon and CACTI, respectively. Panels (b) and (d)
884 show the performance of ceilometer (CEIL) derived PBLH compared to SONDE for
885 the same campaigns. The color gradient indicates the normalized density of data points,
886 while the solid black line represents the line of best fit and error bars indicates the mean
887 and standard deviations for each bin.



888

889 **Figure 12:** Comparative PBLH mean (dots) and standard deviations (error bars) across
890 ARM sites (SGP, GoAmazon, and CACTI). The datasets are derived from radiosonde
891 (SONDE, in black), the DNN model (in pink), ceilometer (CEIL, in blue), and Doppler
892 lidar (DL, in green), respectively. Noted the DL-derived PBLH is only available at the
893 SGP. The percentages in various colors denote the differences in PBLH means derived
894 from the DNN, CEIL, and DL methods relative to SONDE observations. To mitigate
895 sampling bias, these mean values and standard deviations are computed exclusively for
896 intervals where all instruments have concurrently available data.